Nonlinear three-dimensional magnetoconvection around magnetic flux tubes

G. J. J. Botha
Centre for Fusion, Space and Astrophysics, Physics Department, University of Warwick, Coventry CV4 7AL, UK
G.J.J.Botha@warwick.ac.uk

A. M. Rucklidge
Department of Applied Mathematics, University of Leeds, Leeds LS2 9JT, UK
A.M.Rucklidge@leeds.ac.uk

N. E. Hurlburt
Lockheed Martin Solar and Astrophysics Laboratory, Organization ADBS Building 252, Palo Alto, CA 94304, USA
hurlburt@lmsal.com

ABSTRACT

Magnetic flux in the solar photosphere forms concentrations from small scales, such as flux elements, to large scales, such as sunspots. This paper presents a study of the decay process of large magnetic flux tubes, such as sunspots, on a supergranular scale. 3D nonlinear resistive magnetohydrodynamic numerical simulations are performed in a cylindrical domain, initialised with axisymmetric solutions that consist of a well-defined central flux tube and an annular convection cell surrounding it. As the nonlinear convection evolves, the annular cell breaks up into many cells in the azimuthal direction, allowing magnetic flux to slip between the cells away from the central flux tube (turbulent erosion). This lowers the magnetic pressure in the central tube and convection grows inside the flux tube, possibly becoming strong enough to push the tube apart. A remnant of the central flux tube persists with nonsymmetric perturbations caused by the convection surrounding it. Secondary flux concentrations form between the convection cells away from the central tube. The decay of the tube is dependent on the convection around it: convection can remove flux from, add flux to, or change the shape of the central flux tube.

Subject headings: convection — magnetohydrodynamics (MHD) — Sun: interior — Sun: surface magnetism — sunspots

1. Introduction

The appearance of magnetic field on the visible surface of the Sun ranges through many length scales. Magnetic elements surface in the photosphere and are convected to the edges of the convection cells or granules. These elements have a diameter of up to approximately 100 km, a field strength of 1.5 kG and a lifetime of a few minutes (Bello González et al. 2009; Zhang et al. 1998; de Wijn et al. 2009). Where flux elements congregate, as at the boundaries of granules and supergranules, pores form that have diameters between 2 and 4 Mm and field strengths of approximately 2 kG (Bray & Loughhead 1964; Zwaan 1992). These pores have lifetimes of typically less than a day

(Keppens 2001). As magnetic flux accumulates in a pore, it can grow large enough to form a sunspot with a penumbra. Sunspots can be up to 50 Mm in diameter and have life times of a few hours to several weeks. When a sunspot disintegrates, its flux remnants are convected to the polar regions where they are observed as polar elements with diameters of approximately 300 km, field strengths of above 1 kG and lifetimes from several hours to days (Tsuneta et al. 2008; de Wijn et al. 2009). Excellent reviews on all aspects of sunspots are by Solanki (2003) and Thomas & Weiss (2004).

Sunspot decay is often expressed in terms of the temporal evolution of sunspot area. A linear decay rate indicates diffusive processes, while a quadratic decay rate points to erosion of the sunspot by the surrounding convection. Hathaway & Choudhary (2008) looked at the decay rate of sunspot groups and from this calculated the decay rate per individual sunspot. They found that, on average, each sunspot decayed at a rate independent of the area of the spot, i.e. a diffusive process. In contrast, Petrovay & Van Driel-Gesztelyi (1997) looked at individual sunspots and found a parabolic decay rate suggesting erosion by the turbulent convection surrounding the spot. Observations of the outer penumbral boundary shows fluctuations around an average position, indicating an interplay between convective motion and the sunspot's magnetic field (Kubo et al. 2008).

A reasonable approximation for the structure of a pore is a cylindrical magnetic flux tube with inflowing convection surrounding it. Observations of the Sun show patches of strong downflows around the flux concentrations (Hirzberger 2003; Rimmele 2004; Stangl & Hirzberger 2005). Around the edge of pores hair-like striations have been observed with an azimuthal wavelength smaller than the surrounding granular convection (Scharmer et al. 2002; Berger et al. 2004). These striations are believed to be magnetoconvective downflow lanes. Needle-like structures have been observed surrounding pores with an internal flow towards the pore and a downflow at the end near the flux concentration (Sankarasubramanian & Rimmele 2003). A pore growing in size due to accumulated flux may evolve a rudimentary penumbral structure. This proto-penumbra is transitory in nature and may oscillate between penumbral-like filaments and elongated granules (Dorotovič et al. 2002), decay (Sobotka et al. 1999) or evolve into a fully developed sunspot penumbra (Keppens & Martínez Pillet 1996). The formation of a fully formed penumbra around sunspots is usually abrupt, with a sudden change of the magnetic field direction from vertical to inclined (Rucklidge et al. 1995; Yang et al. 2003).

Unlike the flow surrounding pores, a sunspot is surrounded by a moat cell that consists of a surface flow that are flowing predominantly away from the sunspot. The moat flow sometimes exhibits azimuthal structure, with spoke-like lanes of converging flow which have a higher average concentration of outwardly moving magnetic features (Shine & Title 2001; Hagenaar & Shine 2005). Hurlburt & Rucklidge (2000) found in a numerical study of idealised axisymmetric flux tubes in cylinders that a steady collar flow with converging flow at the top of the convection cell is always established around the flux tube. Following Parker's hypothesis (Parker 1979) that a sunspot is a cluster of flux tubes held together by a collar flow, they speculated that sunspots must also have a collar flow. The well-known annular ring of inward moving penumbral grains surrounding a sunspot umbra (Thomas & Weiss 2004) may be explained by three different mechanisms: the first is the emergence of flux tubes through the photosphere (Schlichenmaier et al. 1998); the second by moving patterns caused by granular magnetoconvection in an oblique magnetic field (Hurlburt et al. 1996); and thirdly the presence of a collar flow around the umbra. Observations that the inward radial movement survives the breakup of the penumbra in a decaying sunspot while the umbra stays intact (Deng et al. 2007) support the presence of a collar flow. Helioseismic measurements also support the concept of a collar flow that ensures the integrity of the umbral flux tube (Gizon & Birch 2005; Tong 2005; Zhao et al. 2010). Measurements of p-modes show that underneath the Evershed flow in the penumbra, there exist a converging flow as well as a downflow up to a depth of approximately 3 Mm. Below these flows there is an outflow that extends to more than 30 Mm from the sunspot axis. However, this result is ambiguous because the flow does not appear in f-mode measurements, which give only an outflow to a depth of at least 10 Mm that corresponds to the moat flow on the surface (Gizon & Birch 2005). In addition to this, Moradi

et al. (2010) have shown that different methods of helioseismology give different flow patterns in the subsurface of a sunspot. As a result, the interaction of solar acoustic waves with strong magnetic flux concentrations is actively studied through observations (Braun & Birch 2008), numerical simulations (Shelyag et al. 2009; Parchevsky & Kosovichev 2009) and analytical investigations (Gordovskyy et al. 2009; Jain et al. 2009).

Numerical simulations of magnetoconvection in the upper layer of the solar convection zone follow two complementary strategies. The first is to include as many physical processes as are practical given the numerical constraints. Ionisation, radiative energy transfer and a numerical domain that typically stretches from the temperature minimum in the chromosphere down to a few Mm beneath the visible surface of the Sun have been included in models of three-dimensional (3D) granulation in the quiet Sun (Stein & Nordlund 2006), two-dimensional (2D) flux sheets in an initially unmagnetised, stratified, convecting atmosphere heated from below (Leka & Steiner 2001), 3D pores surrounded by granulation (Cameron et al. 2007), flux emergence of a semi-toroidal loop introduced into a purely hydrodynamic background in statistical equilibrium (Cheung et al. 2010), as well as 3D sunspot umbrae with their penumbrae embedded in the surrounding granulation (Rempel et al. 2009a,b). The second strategic approach to numerical simulations, which is the one we follow in this paper, is to simplify the physics and explore magnetoconvection in this parameter space. As such, our upper domain boundary is 0.5 Mm below the visible surface of the Sun. This allows us to consider the interplay between magnetic field and convection without the complications of sharp gradients due to the stratification. It also means that we cannot say anything about penumbral formation.

The results presented in this paper is a generalisation to three dimensions of 2D (axisymmetric) nonlinear magnetoconvection (Hurlburt & Rucklidge 2000). The axisymmetric results are characterised by a magnetic flux tube at the central axis, with uniform temperature and magnetic field strength inside the tube. Around the flux tube convection cells form concentric rings with the inner ring converging onto the flux tube at the top of the domain, forming a collar flow around the flux tube. The magnetic flux bundle and the convection rings around it are essentially time independent. The larger the radii of the cylindrical numerical domain, the more counter-rotating convection rings form around the central flux bundle. By decreasing the aspect ratio of the cylindrical numerical domain, time dependence was introduced (Botha et al. 2006). For intermediate radii, a small convection ring forming the collar flow establishes itself around the top of the flux bundle, with a dominating counterflow at its outside border. The collar flow is periodically destroyed by the counterflow and reforms. During this process the magnetic field expands radially in the absence of the collar flow and is pushed back into a tight flux bundle on the central axis upon the reformation of the collar flow. Botha et al. (2008) showed that when the numerical domain is rotated, a Rankine vortex forms: the magnetic flux tube rotates as a rigid body while sheared azimuthal flow (i.e. a free vortex) forms in the surrounding convection cells.

In this paper the robustness of a magnetic flux tube surrounded by 3D nonsymmetric convection is presented. It is shown that a remnant of the original flux tube persists in spite of these nonsymmetric perturbations, with secondary flux concentrations forming around the remnant. The secondary concentrations form due to magnetic flux escaping from the central flux bundle, and their strength depends on an interplay between the strength of the magnetic field in the simulation and the vigour of the convection. In the simulations we have used magnetic field strengths of $Q = 32$, 100 and 250, where Q is the Chandrasekhar number. The numerical domain is a cylindrical wedge with an aspect ratio varying between 3 and 6.

This study of 3D nonlinear convection was preceded by initialising the numerical simulations with a time independent (nonlinear) 2D solution and perturbing the plasma in the azimuthal direction (Botha et al. 2007). The linear evolution of these perturbations showed that steady and oscillating instabilities with a preferred azimuthal number formed in the convecting flow close to the outer edge of the flux tube. A concise summary and expansion of these results are given in Section 4 before the discussion moves on to the nonlinear magnetoconvection results that form the bulk of this paper.

The paper first discusses the model in the next section, and then describes the design of the numerical experiments and their initialisation (Section 3). The evolution of the linear azimuthal modes is summarised in Section 4, before the nonlinear results are presented in Section 5. In the discussion we consider the influence of an increasing Chandrasekhar number (Q) on the results, as well as the effect of the azimuthal width of the numerical domain (Section 5.1) and a changing aspect ratio (Section 5.2). The paper concludes with a discussion and short summary of the results (Sections 6 and 7).

2. Model

The initial temperature and density profiles in the vertical (z) direction are given by the polytrope

$$T = T_0(1+\theta z), \quad (1)$$
$$\rho = \rho_0(1+\theta z)^m, \quad (2)$$

with the 0 subscript defining the quantity at the top of the box ($z = 0$), θ is the initial temperature gradient, and m is the polytropic index. The equations for fully compressible, nonlinear three-dimensional (3D) magnetoconvection are

$$\frac{\partial \rho}{\partial t} = -\nabla\cdot(\mathbf{v}\rho) \quad (3)$$

$$\frac{\partial \mathbf{v}}{\partial t} = -\mathbf{v}\cdot\nabla\mathbf{v} + \theta(m+1)\hat{\mathbf{z}} + \frac{\sigma\zeta_0 K^2 Q}{\rho}\mathbf{j}\times\mathbf{B} - \frac{1}{\rho}\nabla P + \frac{\sigma K}{\rho}\left(\nabla^2\mathbf{v} + \frac{1}{3}\nabla\nabla\cdot\mathbf{v}\right) \quad (4)$$

$$\frac{\partial T}{\partial t} = -\mathbf{v}\cdot\nabla T - (\gamma-1)T\nabla\cdot\mathbf{v} + \frac{\gamma K}{\rho}\nabla^2 T + \frac{\zeta_0}{\rho}\left|\mathbf{j}\right|^2 \quad (5)$$

$$\frac{\partial \mathbf{B}}{\partial t} = \nabla\times(\mathbf{v}\times\mathbf{B}) + \zeta_0 K\nabla^2\mathbf{B} - \nabla\psi \quad (6)$$

with the auxiliary equations

$$P = \rho T, \qquad \mathbf{j} = \nabla\times\mathbf{B}. \quad (7)$$

The variable ψ is introduced to enforce the condition $\nabla\cdot\mathbf{B} = 0$ (Dedner et al. 2002), and it evolves through

$$\frac{\partial\psi}{\partial t} = -c_h^2\nabla\cdot\mathbf{B} - \frac{c_h^2}{c_p^2}\psi, \quad (8)$$

where c_h and c_p are constants. We use the following notation: γ the ratio of specific heats; σ the Prandtl number; ζ_0 the magnetic diffusivity ratio at $z = 0$; and Q is the Chandrasekhar number. The dimensionless thermal conductivity K is related to the Rayleigh number R in the following way:

$$R = \theta^2(m+1)\left[1 - \frac{(m+1)(\gamma-1)}{\gamma}\right]\frac{(1+\theta/2)^{2m-1}}{\sigma K^2} \quad (9)$$

R is a measure of the importance of buoyancy forces compared to viscous forces in the middle of the layer. All the other symbols have their usual meaning. The physical quantities are dimensionless, with the length scaled proportional to the depth of the numerical domain, velocities scaled proportional to the sound speed at the top of the domain and temperature, magnetic field, density, and pressure all scaled proportional to their initial values at the top of the numerical domain, so $T_0 = 1$ and $\rho_0 = 1$.

The numerical implementation of the model was developed specifically for these types of calculations (Hurlburt & Rucklidge 2000). The cylindrical grid is in the shape of a wedge with dimensions

$$0 \le r \le \Gamma, \quad 0 \le \phi \le 2\pi/M_\phi, \quad 0 \le z \le 1, \quad (10)$$

with $z = 0$ at the top of the domain. Sixth-order compact finite differencing is used in the vertical (r, z) plane and the domain has a spectral azimuthal (ϕ) direction. The level of dealiasing is increased toward the central axis to maintain grid uniformity. For time evolution we use a fourth-order modified (explicit) Bulirsch-Stoer integration technique. The number of grid points in the radial direction is typically $64\times\Gamma$, in the vertical direction 64, and in the azimuthal direction between 64 and 512.

The boundary condition in the azimuthal direction is periodic. At the central axis we impose regularity conditions and the domain has a slippery, perfectly conducting, thermally insulating outer wall. The way that we impose on-axis regularity conditions constrains the value of M_ϕ to be at least 4. Both the top and bottom boundaries are impenetrable, with a vertical magnetic field and with their respective temperatures fixed. The boundaries are described in detail in Botha et al. (2006).

3. Initialisation and design of numerical experiments

All the numerical results in the paper were obtained with the following parameter values: $R = 10^5$, $\sigma = 1$, $\zeta_0 = 0.2$, $\theta = 10$, $\gamma = 5/3$ and $m = 1.495$. The values of the Chandrasekhar number Q, the azimuthal width M_ϕ and the radius Γ were varied and will be reported throughout the paper. These physical parameter values were chosen to describe the solar convection zone from a depth of approximately 0.5 Mm below the visible surface of the Sun to a depth of approximately 6 Mm (Botha et al. 2006). The numerical domain is a cylindrical wedge of one unit deep and a radius of $\Gamma \geq 3$, so that the simulations are on a supergranular scale. It is worth pointing out that the value of the Prandtl number used here is much larger than the value of σ in the upper layer of the solar convection zone. In axisymmetric simulations we have used $\sigma = 1$ and $\sigma = 0.3$ (Botha et al. 2008). The result was the same qualitatively, displaying more vigorous convection in the case of lower σ. The same was found for the 3D numerical simulations presented in this paper. The stronger convection forced smaller time steps and denser numerical grids, so that we used $\sigma = 1$ for expediency in all the results presented here.

The three-dimensional simulations are initialised with an axisymmetric, or two-dimensional, solution as shown in Figure 1. It consists of a well defined flux tube at the central axis with a convection cell around it, forming an annular collar flow that contains the magnetic flux at the central axis. This solution was obtained by starting 2D simulations with a uniform field and a velocity perturbation. Galloway, Proctor & Weiss (1978) showed that for an incompressible Boussinesq fluid with vertical top and bottom magnetic boundaries, the magnetic flux is concentrated almost entirely at the central axis. Previous numerical results show that this is also true for compressible fluids, with the width of the numerical box determining the number of convection cells forming around the flux bundle (Hurlburt & Rucklidge 2000). We have taken care to allow only one convection cell to form, by adapting the value of Q to the size of the domain. The stronger magnetic field in the case of higher Q values causes a wider flux bundle to form at the centre, in this way allowing us to regulate the remaining space in which convection forms.

The linear phase of the 3D simulations were started by perturbing the vertical component of the velocity in the azimuthal direction. The perturbation took the form of a cosine wave with wavelength equal to the azimuthal width of the numerical domain. By changing the width of the wedge, we were able to measure the growth rates of different wavelengths (Botha et al. 2007). The solution with the largest linear growth-rate was then chosen to continue into the nonlinear regime. In order to test the robustness of the nonlinear results obtained in this manner, we also initialised 3D simulations with a uniform vertical magnetic field. Flux separation occurred and eventually these results were indistinguishable from the nonlinear results obtained as described above, provided that certain conditions were met, as discussed in Section 5.2.

4. Linear azimuthal evolution

In the linear phase the solution forms a static axisymmetric standing wave inside the magnetic flux tube, and one annular convection cell around the tube, as shown in Figure 2(a). The density profile of the solution is hardly perturbed from the polytrope, because the atmosphere is close to adiabatic, i.e. m is close to $1/(\gamma-1)$. In order to obtain the location of the linear eigenmodes, we take the azimuthal perturbation of the physical quantities, as shown in Figure 2(b). It is clear that the linear modes are situated at the edge of the magnetic flux tube. This was confirmed by sampling the data in the horizontal midplane of the numerical domain. The azimuthal size of the linear modes is related to the size of the magnetic flux tube. Figure 3 shows that for small tube radii the linear azimuthal lengths are short. As the tube radius increases, its influence on the azimuthal length scale decreases. The result is a well-defined length scale in the limit of large radii. This is a geometric effect, with the azimuthal length of the local linear mode dependent on the curvature of the tube radius that it samples.

The radius of the numerical domain has an influence on the growth-rate of the linear modes. Figure 4 shows that for a larger radius, the maximum growth rate is higher when all other physi-

cal parameters are kept the same. This is consistent with the explanation that larger aspect ratios allow the convection in the solution to be more dominant, as discussed in Section 5.2. Botha et al. (2007) determined that the eigenfunctions of the linear modes forming around the magnetic flux tubes are convective in nature. As in that paper, we found linear modes with steady growth and modes with oscillating growth. The steadily growing modes tend to occur at low values of M_ϕ. There is a suggestion in the data that the period of the oscillating modes are shorter the more they penetrate into the magnetic flux tube. However, difficulty in establishing the edge of the magnetic flux tube as well as the time dependence of the solution prevented us from obtaining a scaling law between mode penetration and oscillation frequency.

5. Nonlinear azimuthal evolution

As the solution moves from the linear into the nonlinear regime, the annular convection cell around the magnetic flux tube breaks up into many cells. The absence of a uniform collar flow allows the magnetic field to expand into the areas between the convection cells, which in turn lowers the magnetic field strength near the central axis ($r = 0$). Lower magnetic strength inside the flux tube means that low levels of convection are allowed to form, the maximum amplitude of which depends on the magnetic field strength in the numerical domain.

For $Q = 32$ the axisymmetric initial condition is a narrow vertical flux tube at the central axis. In this case a slight increase in tube radius allows for a relatively large decrease in magnetic field strength. It follows that after a small amount of magnetic field has moved between the convection cells surrounding the central flux tube, convection forms inside the tube that grows and becomes strong enough to break it up. The end result is magnetic flux between the convection cells with only a flux tube remnant at the central axis. This final state is shown in Figure 5 at a time when the nonlinear magnetoconvection is well established.

In the case of $Q = 100$, the axisymmetric initial condition consists of a central magnetic flux tube that is wider than the case for $Q = 32$. As soon as the annular convection cell around the flux tube starts to break into many cells, magnetic flux moves between the cells radially away from the central axis. The relative change in the magnetic field at the central axis is less than for $Q = 32$ and weaker convection forms inside the flux tube. As a consequence, it takes longer for the convection to erode the magnetic field away from the central axis. Eventually a steady nonlinear state forms with magnetic flux between the convection cells and with a reduced central magnetic flux tube. Figure 6 shows the result for $Q = 100$ and $\Gamma = 3$. As the solution evolves through time, the magnetic flux is pushed around by the convection. In particular, the flux forming the central tube is buffeted by strong irregular convection. This leads to the central flux tube changing shape, with radial tendrils forming temporarily between the convection cells surrounding the flux tube.

Figure 7 shows the result for $Q = 250$ when the nonlinear magnetoconvection is well established. Compared to the axisymmetric initial condition, the radius of the magnetic flux tube is only slightly larger when nonlinear magnetoconvection is established. This means the weak convection forming inside the flux tube is not strong enough to push magnetic flux away from the central axis. The edge of the magnetic flux tube is buffeted by the convection around it, as in the case for $Q = 100$, but fewer radial tendrils form between the convection cells and those that do form are weaker than in the case when $Q = 100$. In order to see the same breakup of the magnetic tube as for $Q = 32$, one has to enlarge the radius of the numerical domain (Γ) so that the magnetic flux has more room to disperse between the convection cells and in the process lowers the magnetic field strength at the central axis. The influence of a larger Γ is considered in Section 5.2.

A quantitative measure of the breakup of the central magnetic flux tube is provided by defining the radial profile of the magnetic field as

$$|\bar{B}(r)| = \frac{1}{nz.n\phi} \sum^{nz} \sum^{n\phi} \sqrt{B_r^2 + B_\phi^2 + B_z^2}\,, \quad (11)$$

where nz and $n\phi$ are the number of data points in the vertical and azimuthal directions respectively. This gives an indication of the size of the magnetic field in the radial direction, i.e. the magnetisation of the plasma as a function of the radius.

Figures 5(d), 6(d) and 7(d) give the radial profiles of $|\bar{B}| = |\bar{B}(r)|$ for $Q = 32$, $Q = 100$ and $Q = 250$ respectively at different times during the numerical simulations. All of them show a well-defined magnetic flux tube at the central axis at the axisymmetric initial condition. The annular ring around the central flux tube breaks up into many cells in the azimuthal direction for all values of Q. In the case of $Q = 32$ and $Q = 100$, two concentric circles of cells form around the magnetic flux tube. This allows magnetic flux to move between the cells in the radial direction and to be captured between the cells at a radial position of approximately $r = 1.7$. The value of the magnetic field at these positions are similar for $Q = 32$ and $Q = 100$, as shown in Figures 5(d) and 6(d). These figures also show the relatively large decrease of magnetic field at the central axis for $Q = 32$ and the lesser decrease for $Q = 100$. In the case of $Q = 250$ only one ring of convection cells forms around the magnetic flux tube. Figure 7(d) shows that the magnetic flux tube radius increases slightly, as only a small amount of flux moves between the convection cells. The magnetic field inside the flux tube decreases less than in the case for $Q = 100$, so that weaker convection forms inside the flux tube and the tube stays intact throughout the simulation run.

Where strong flows carve into the central magnetic tube, the magnetic field is pushed together and the field strength experiences a local peak value. This can be seen in Figure 7(a) for $Q = 250$. At the edge of the flux tube, indentations into the tube is caused by strong convection pushing against the side of the tube. The magnetic field is also stronger at these indentations than at the protrusions between them, where the magnetic field pushes into weaker convection flows.

The interplay between the central magnetic flux tube and the convection surrounding it can be seen in Figure 8, where the time evolution of $|\bar{B}| = |\bar{B}(r)|$ is shown for the different values of Q. Figure 8(a) shows that for $Q = 32$ at time 600, the convection inside the magnetic flux tube becomes strong enough to push a significant part of the magnetic flux away from the central axis. In contrast, $Q = 250$ in Figure 8(c) has a magnetic field that is strong enough to keep the magnetic flux tube intact, in spite of weak convection that forms inside the flux tube. In the case of $Q = 100$, Figure 8(b) shows that weak convection starts at time 550. Eventually the convection grows strong enough to push magnetic flux away from the central flux tube, so that at time 1000 the nonlinear magnetoconvection with $Q = 32$ and with $Q = 100$ look similar.

The magnetic flux that escapes from the central flux tube tends to congregate at strong downflows between convection cells where the convection is converging. In the region where the convection dominates, this is between the convection cells where strong downflows occur. Figure 9 shows the region of convection in green, and the locations of strong magnetic field in blue. One clearly observes the magnetic flux remnant at the central axis through the absence of convection as well as the magnetic field concentrated there. The downward plumes in the convection can be seen with their associated strong magnetic field concentrations. It is noticeable that the magnetic field strength in the plumes is maximum in the top half of the numerical domain, while the downward velocities reaches their maximum in the bottom half of the domain. The chaotic convection near the bottom boundary in Figure 9 is a consequence of our impenetrable boundary condition and is not relevant to the current discussion. Where the magnetic field peaks, either at the central axis or in the downward plumes, an azimuthal current forms a ring around the magnetic field concentration. This is shown in the vertical planes of Figures 5, 6 and 7 for all values of Q.

Figure 10 shows the close relation between the convection and the temperature in the solution. Everywhere an upflow occurs, the plasma is hot relative to the surrounding temperature. As a result, the temperature perturbation on every plane shows clearly the forms of the convection cells, as can be seen in the top part of the numerical domain. At the plumes, where strong downflow occurs, the plasma is cool relative to the surrounding temperature. Figure 10 shows the downflows together with their associated lower temperature near the bottom of the domain.

The radius of the numerical domain allows two concentric rings of convection cells to form in the case of $Q = 32$ and $Q = 100$, shown in the vertical planes of Figures 5 and 6. The cell closest to the central axis has an upflow next to the magnetic flux tube, while the outer cell has an upflow

next to the outer boundary. These strong upflows, together with the strong downflows between the convection cells, are observable in the 3D rendering of the vertical velocity component in Figure 10 for $Q = 100$. For $Q = 250$ only one ring of convection cells forms, as can be seen in the vertical planes shown in Figure 7.

In previous axisymmetric simulations of a central flux tube surrounded by convection, an annular cell flowing towards the flux tube at the top of the numerical domain was always present to keep the flux tube intact (Hurlburt & Rucklidge 2000). In the absence of this collar flow the magnetic flux tube spread out radially until the collar flow was restored (Botha et al. 2006). We observe the same phenomenon in three dimensions. Figure 7 shows one inward flowing collar cell that keeps the magnetic flux tube confined to the central axis, with very little magnetic field present in the convection. In contrast, the outward flowing cells of $Q = 32$ and $Q = 100$ in Figures 5 and 6 allow magnetic flux to escape from the flux tube. It is interesting that the flux tube is not completely destroyed in these cases. A remnant of the tube is left at the central axis, which becomes more prominent as the value of Q increases.

The Alfvén speed in the model is defined as $c_A^2 = \sigma\zeta_0 K^2 Q B^2/\rho$. Figure 9 shows that the highest values of the magnetic field occurs at the top of the downflows. This is true for both $Q = 32$ (Figure 5) and $Q = 100$ (Figures 6 and 9). Consequently these are also the locations for the highest values of c_A in the numerical domain, since the density increases as one moves downwards.

5.1. Effect of wedge width

The effect of the wedge width on the nonlinear results is investigated by doubling the azimuthal angle of the numerical domain from $M_\phi = 8$ to $M_\phi = 4$ and then continuing the simulation run. Figure 11 shows the result for $Q = 32$. In this case the convection cells merge from two concentric circles, each with eight cells in the azimuthal direction, to one concentric circle consisting of four cells in the azimuthal direction. Figure 12 shows how initially part of the magnetic field is trapped between the convection cells, which then moves towards the central axis as the convection pattern changes from two concentric circles to one. Three instances from Figure 12 are plotted in Figure 11(d), with the final state showing that most of the magnetic field are being pushed towards the central axis.

The initial state of this simulation is similar to that depicted in Figure 5. Here the convection forms two concentric circles of eight cells each in the azimuthal direction, with orientation such that the inner radial cells flow radially outward and the outer cells radially inward at the top of the domain, as can be seen in Figures 5(b) and (c). During the simulation the inner cells become weaker while the outer cells grow stronger (Figure 12). The final state in the wider wedge is shown in Figure 11. Figure 11(c) shows the large convection cells that formed, with strong flow moving inward at the top of the domain. Figure 11(b) shows a region on the boundary between the large convection cells. Here one finds weaker convection and a magnetic field that is pushed between the two cells away from the central axis, so that the width of the central flux tube is larger here than at positions where the strong convection forces the magnetic flux against the central axis. This is clearly visible in Figures 11(a), (b) and (c).

For $Q = 100$ and $Q = 250$ the number of cells in the radial and azimuthal directions stays the same when the numerical domain is widened. Figure 13 shows the simulation result when $Q = 250$. This behaviour can be explained by considering the geometry of the solution. A convection cell naturally wants to maintain a shape where its radial size is approximately the same as its azimuthal size. For low values of Q, the magnetic flux tube has a small radius and the numerical domain containing the convection a large one. In a narrower wedge, as in Figure 5 for $Q = 32$ and $M_\phi = 8$, the size of convection cells is limited by constraints in the azimuthal direction. This means that two cells form in the radial direction, each of which has approximately the same radial diameter as its azimuthal diameter. By doubling the wedge width, as in Figure 11, this constraint is lifted so that the azimuthal width becomes approximately the same as the radial width of the convective area in the numerical domain. Consequently one cell forms that fit into the radial as well as the azimuthal directions. For $Q = 250$ the magnetic flux tube fills half the radius of the domain, while the other half contains the convection (Figure 13). In this case the radial width of one convection cell fits

eight times into one full azimuthal rotation. As a consequence, doubling the width of the numerical domain has no effect on the number of cells forming around the magnetic flux bundle. We conclude that as long as the radial width of the convection area (r_c) is smaller or of equal size to the azimuthal width of the numerical domain, i.e.

$$r_c \leq \frac{2\pi r_p}{M_\phi}, \tag{12}$$

where r_p is the radius of the magnetic flux tube, then the width of the domain will not restrict the formation of cells in the convection around the flux tube.

5.2. Initial conditions and aspect ratio

In order to determine the influence of the design of the numerical experiments (Section 3) on the nonlinear results, we initialised the 3D numerical domain with a uniform vertical magnetic field and a velocity perturbation. For a radius of $\Gamma = 3$ and a wedge width of $M_\phi = 8$, the numerical results are indistinguishable from the results described in this paper (Figures 5, 6 and 7), provided that the duration of the run is long enough for flux separation to occur and for the flux to migrate through the convective region and accumulate at the central axis.

To investigate the role of the radius of the numerical domain, we doubled the radius to $\Gamma = 6$ and repeated the runs from an initial uniform vertical magnetic field. These nonlinear final states are shown in Figures 14 and 15. Nonlinear convection forms within 200 time units after initialisation, as can be seen in Figure 16. The number of convection cells is determined by the ratio of their radial and azimuthal widths being close to one. This means that in the case of $M_\phi = 8$ the limited azimuthal width forces many convection cells to form in the radial direction. In the case of $Q = 32$ the convection is strong enough for five concentric circles of counter-flowing convection cells to form around the central axis, with three downflow regions between them, as shown in Figure 14(a). For larger values of Q, the stronger magnetic field causes this pattern to break up, as seen in Figures 14(b) and 15.

Flux separation occurs with magnetic flux congregating at the downflow locations between convection cells, as shown in Figures 14(a), 14(b) and very clearly at midradius in Figure 15(b). Starting from a vertical field, the magnetic flux is caught between convection cells and never migrates to the central axis. Hence at all times there is a substantial amount of flux in the whole of the domain, shown in Figures 14(c) and 14(d) for $Q = 32$ and $Q = 250$ respectively. This should be compared with the cases for radius $\Gamma = 3$, shown in Figures 5(d) for $Q = 32$ and 7(d) for $Q = 250$. For the smaller radius fewer convection cells form along the radial direction of the numerical domain, which means the number of downflows between cells in the convection where magnetic flux congregates are less. However, the amount of flux at a downflow location is approximately the same for both $\Gamma = 3$ and 6, as can be seen when the peak values of $|\bar{B}| = |\bar{B}(r)|$ at downflows are compared in Figures 5(d) and 14(c) for $Q = 32$ and Figures 7(d) and 14(d) for $Q = 250$.

It is worth comparing the start of simulations with a uniform magnetic field for radii $\Gamma = 3$ and $\Gamma = 6$. In both cases an initial central flux tube forms that is short-lived in the case for $\Gamma = 6$ with $Q \geq 100$, as shown in Figures 16(b) and (c). The turbulent flow erodes magnetic flux away from the central axis and pushes the magnetic flux around inside the numerical domain so that no central flux tube forms during the simulations, as shown in Figure 14(d) for $Q = 250$. The evolution of this process can be seen in Figures 16(b) and (c). For $Q = 32$ and $\Gamma = 6$ the initial central flux tube survives longer, but eventually is eroded away by strong convection cells that form next to it, as shown in Figure 16(a). In contrast, for a radius of $\Gamma = 3$ the central flux tube that initially forms is much more resilient. This is because radially only two convection cells form around it when $Q = 32$ (Figure 5) and $Q = 100$ (Figure 6), while only one cell fits into the radius when $Q = 250$ (Figure 7). There are fewer opportunities for the magnetic flux to move between convection cells away from the central axis when compared to the case when $\Gamma = 6$. The final states initialised with a uniform magnetic field are indistinguishable from Figures 5, 6 and 7, in spite of the fact that the results in these figures evolved from a central flux tube with one annular convection cell around it, as shown by Figure 8.

In the case of a vertical field initialisation with radius $\Gamma = 6$, the majority of the magnetic flux

does not migrate through the convective region to congregate at the central axis, in contrast with a vertical field initialisation with radius $\Gamma = 3$. This can be seen when Figures 5(d) and 14(c) are compared for $Q = 32$, as well as Figures 7(d) and 14(d) for $Q = 250$. The fact that more convection cells form in the larger numerical domain when $\Gamma = 6$ means that more magnetic flux is trapped between the cells, rather than being pushed towards the central axis. As the value of Q increases, the convection finds it more difficult to push magnetic flux around, so that time-dependent patterns evolve. Thus one moves from strong convection and a small magnetic flux concentration at the centre for $Q = 32$, shown in Figures 14(a) and (c), to a very strong magnetic field that completely dominates the convection. We have done simulations up to $Q = 700$ and this statement holds true over the whole range of Q. This phenomenon was also observed by Hurlburt & Alexander (2002). Figures 14(b) and (d), together with Figure 15, show the case when $Q = 250$. Here the interplay is such that convection cells form between significant concentrations of magnetic flux throughout the domain.

The prominent narrow peak in the magnetic flux near $r = 0$ that forms towards the end of the simulation in Figure 14(c) when $\Gamma = 6$ and $Q = 32$, can be ascribed to a strong convection cell that forms close to the central axis and that pushes some of the magnetic flux against $r = 0$. This is clearly visible in Figure 16(a) that shows the time evolution of $|\bar{B}| = |\bar{B}(r)|$. In fact, Figure 16 shows that this process occurs repeatedly throughout the numerical simulations for all values of Q. Convection cells form close to the central axis, which erode some of the flux away from the central axis while pushing the remnant closer to the central axis. Comparing Figure 16 when $\Gamma = 6$ with Figure 8 when $\Gamma = 3$, it is clear that the erosion of the magnetic field caused by the convection cells will prevent a flux bundle forming at the central axis. However, this is only true when the radius of the numerical domain is sufficiently large for more than two concentric circles of convection cells to form. In the case for $\Gamma = 3$, the final state of a central flux bundle with convection surrounding it was obtained with an initialisation using an axisymmetric central flux tube (as in Figure 8) as well as an initialisation with a uniform vertical field.

6. Discussion

This paper can be thought of as an exploration of two physical processes: flux separation and turbulent erosion. Flux separation occurs when turbulent eddies expel magnetic flux to their borders where the flux concentration builds up (Weiss 1966), while turbulent erosion is the process when convection cells push against magnetic flux concentrations and allow the flux to escape between them away from the area of high concentration (Simon & Leighton 1964).

The 2D axisymmetric solutions used as initial conditions for the 3D numerical simulations presented here, have a well-defined magnetic flux tube at the central axis with an annular convection cell around it (Figure 1). Irrespective of the radius of the domain, i.e. the number of counter-rotating convection cells that fit into the domain, almost all the magnetic flux in the solution gathers at the central flux bundle (Hurlburt & Rucklidge 2000). This final state is maintained indefinitely.

As soon as a third dimension is introduced to the axisymmetric solution, the annular convection cell breaks up in the azimuthal direction into convection cells that have approximately equal radial and azimuthal diameters (Figures 5, 6 and 7). The dimensions of the convection cells were discussed in Section 5.1. The convection cells that push against the central magnetic flux tube push some of the magnetic flux between them, which reduces the magnetic pressure inside the flux tube. This allows weak magnetoconvection cells to form inside the tube, which can grow strong enough to break the flux tube up through flux separation (Figure 8). A remnant of the original flux tube remains at the central axis, while the rest of the magnetic flux is captured between the convection cells in the numerical domain.

Most of the magnetic flux between cells gather at the locations of the strongest downflows (Figure 9). These downflowing plumes are well known from Cartesian simulations of magnetoconvection (Cattaneo et al. 2003). They exhibit strong magnetic flux concentrations in the top layers of the numerical domain. The velocity increases as the flow moves downward along the plume. The magnetic flux gathering at these locations are not

strong enough to influence the convection pattern around them. As a result, the flux concentrations are easily manipulated and destroyed by the convection surrounding them, similar to the final destruction of solar pores as observed by Sobotka et al. (1999).

The central magnetic flux bundle is weakened by flux slipping away from it between the convection cells that exist around the flux bundle. This process is highly dynamic, with temporary finger-like protrusions forming between the cells, to be destroyed again when the magnetoconvection pushes them back to the central axis. Petrovay & Moreno-Insertis (1997) solved the 2D axisymmetric diffusion equation with a diffusivity dependent on the magnetic field, to show that a magnetic flux tube decays from its outer edge to its centre, in the process forming a sharp gradient at its edge. They also found that a fraction of the magnetic flux tube always remains. This idealised result will be true when small convection cells surround a large magnetic flux bundle. In the results we presented in this paper, eight convection cells (Figure 5) as well as four convection cells (Figure 11) leave a flux bundle remnant at the central axis, provided that the radius of the numerical domain is small in order to limit the amount of convection cells forming.

Unlike the idealised diffusion result of Petrovay & Moreno-Insertis (1997), the decay of the central flux bundle is not a steady process, but highly dependent on the nonlinear magnetoconvection surrounding the flux bundle. As convection cells form inside the magnetic flux bundle, they push the flux away from the central axis (Figure 8). The opposite process occurs when convection cells are destroyed next to the central flux bundle. In this case the magnetic flux that was captured between the cells is pushed towards the central axis, thus increasing the radius of the magnetic flux bundle (Figure 12). Thus the decay of the central magnetic flux tube is dominated by magnetoconvection (Figures 8 and 16) and we cannot fit a linear or parabolic decay rate to these numerical results. Another possible influence of the convection on the magnetic structure occurs when weak convection forms inside the magnetic flux bundle. If the convection is too weak to destroy the integrity of the flux bundle, it only increases the diameter of the flux bundle slightly, as shown in Figure 8(c).

In this paper we also considered the question of whether a central magnetic flux bundle will form spontaneously when starting from a uniform vertical magnetic field in a cylindrical (3D) numerical domain (Section 5.2). For a radius of $\Gamma = 3$ the final state is indistinguishable from the final state when the numerical simulation is initialised with an axisymmetric flux bundle at the centre. For this radius some of the magnetic flux is captured between the convection cells, but a significant proportion of the flux is pushed to the central axis, as shown in Figures 5(d), 6(d) and 7(d). However, when the radius is lengthened to $\Gamma = 6$, it is more difficult to distinguish between flux that is captured between the convection cells and flux that forms the central bundle, as shown in Figures 14(c) and (d). Indications are that the magnetoconvection continuously removes flux from the central axis through new convection cells forming at the edge of the flux bundle and pushing flux away from the central axis through flux separation (Figure 16). For larger radii we expect that even less magnetic flux will be available to form a central axis, as more flux will be captured between convection cells that form in the numerical domain.

7. Conclusion

This paper presents numerical simulations of magnetic flux tubes in a 3D cylindrical domain, solving the nonlinear resistive magnetohydrodynamic equations. The simulations were initialised with an axisymmetric (2D) solution consisting of a central magnetic flux tube and one annular convection cell around it. The solution was then perturbed with an azimuthal velocity perturbation.

Linear modes form in the azimuthal direction, situated on the border between the central flux tube and the convection cell. During the linear stage of the developing azimuthal perturbation, the wavelength of the fastest growing mode depends on the radius of the central magnetic flux tube. For small tube radii the wavelength is small, while it increases as the tube radius increases. However, the dependence of the mode length on the tube radius decreases as the tube radius increases, so that there exist a well-defined length scale in the limit of large radii.

When the nonlinear three-dimensional convec-

tion develops, the annular cell breaks up into many cells. Magnetic flux slips between the cells away from the central flux tube. This process is known as turbulent erosion. The magnetic pressure in the central tube becomes less and convection grows inside the flux tube that can become strong enough to push the tube apart. A remnant of the central flux tube persists, undergoing nonsymmetric perturbations caused by the convection surrounding it. The size of the central tube remnant and its perturbations both depend on the interplay between the magnetic field and the convection. For $Q = 32$, strong convection forms at the edge of the flux tube that pushes flux away from the central tube. For $Q = 100$ weaker convection forms inside the tube that takes longer to reached the same final state as when $Q = 32$. For $Q = 250$ convection forms inside the flux tube that is too weak to break the integrity of the tube.

The decay of the tube is dependent on the convection around it. The convection can remove flux from the tube when new convection cells form inside the flux tube, or add flux to the tube when convection cells next to the flux tube are destroyed and flux caught between the convection cells is pushed back to the central tube. The convection can also change the shape of the central flux tube by pushing against the magnetic flux so that some of the flux is pressed in between convection cells. In this way during the simulations, finger-like protrusions develop between the convection cells that surround the central flux tube. These are time dependent, forming and disappearing as the convection pattern around the central flux tube changes.

Secondary flux concentrations form between the convection cells away from the central tube. This occurs at temporary downflowing plumes that form between convection cells where the convection converges.

Some simulations were initialised with a uniform vertical magnetic field and allowed to develop nonlinear magnetoconvection. For smaller radii ($\Gamma = 3$) results were obtained that are indistinguishable from when the simulations were initialised with an axisymmetric central flux tube. For larger radii ($\Gamma = 6$) more convection cells formed in the numerical domain, which captured more of the magnetic flux in the downflows between them. As a result, the flux concentration at the central axis was less defined.

The conclusion from the work presented in this paper is that the decay of a central flux tube is dictated by the nonlinear magnetoconvection surrounding it. The formation and destruction of convection cells around the flux tube can add or subtract magnetic flux from the tube. As such, the flux tube's decay rate does not fit a simple law. A remnant of the central flux tube always survives, with secondary flux concentrations between the convection cells. The more convection cells form, the more flux is captured between the cells and the central tube becomes less defined.

GJJB and AMR would like to acknowledge financial support from NASA grant NNG04GG07G, PPARC grant PPA/G/O/2002/00014 and STFC grants PP/E001092/1, ST/F00205X/1 and ST/H002332/1. NEH would like to acknowledge support from NASA grants NNG06GD45G and NNM07AA01C. Computing facilities were provided by the White Rose Grid and the NASA supercomputer, the latter made possible through Prof. F.H. Busse.

REFERENCES

Bello González, N., Yelles Chaouche, L., Okunev, O., & Kneer, F 2009, A&A, 494, 1091

Berger, T. E., Rouppe van der Voort, L. H. M., Löfdahl, M. G., Carlsson, M., Fossum, A., Hansteen, V. H., Marthinussen, E., Title, A., & Scharmer, G. 2004, A&A, 428, 613

Botha, G. J. J., Rucklidge, A. M., & Hurlburt, N. E. 2006, MNRAS, 369, 1611

Botha, G. J. J., Rucklidge, A. M., & Hurlburt, N. E. 2007, ApJ, 662, L27

Botha, G. J. J., Busse, F. H., Rucklidge, A. M., & Hurlburt, N. E. 2008, MNRAS, 387, 1445

Braun, D. C., & Birch, A. C. 2008, Sol. Phys., 251, 267

Bray, J. R., & Loughhead, R. E. 1964, Sunspots, Chapman and Hall, London

Cameron, R., Schüssler, M., Vögler, A., & Zakharov, V. 2007, A&A, 474, 261

Cattaneo, F., Emonet, T., & Weiss, N. O. 2003, ApJ, 588, 1183

Cheung, M. C. M., Rempel, M., Title, A. M., & Schüssler, M 2010, ApJ, 720, 233

de Wijn, A. G., Stenflo, J. O., Solanki, S. K., & Tsuneta, S. 2009 Space Sci. Rev., 144, 275

Dedner, A., Kemm, F., Kröner, D., Munz, C.-D., Schnitzer, T., & Wesenberg, M. 2002, Journal of Computational Physics, 175, 645

Deng, N., Choudhary, D. P., Tritschler, A., Denker, C., Liu, C., & Wang, H. 2007, ApJ, 671, 1013

Dorotovič, I., Sobotka, M., Brandt, P. N., & Simon, G. W., 2002, A&A, 387, 665

Galloway, D. J., Proctor, M. R. E., & Weiss, N. O. 1978, Journal of Fluid Mechanics, 87, 243

Gizon L., Birch A. C., 2005, Living Rev. Solar Phys., 2, 6. Online Article: cited 9/01/2006, http://www.livingreviews.org/lrsp-2005-6

Gordovskyy M., Jain, R., & Hindman, B. W. 2009, ApJ, 694, 1602

Hagenaar, H. J., & Shine, R. A. 2005, ApJ, 635, 659

Hathaway, D. H., & Choudhary, D. P. 2008, Sol. Phys., 250, 269

Hirzberger, J. 2003, A&A, 405, 331

Hurlburt, N. E., Alexander, D. 2002, in COSPAR Colloq. 14, Solar-Terrestrial Magnetic Activity and Space Environment, ed. H. Wang & R. Xu (Oxford: Pergamon), 19

Hurlburt, N. E., Matthews P. C., & Proctor, M. R. E. 1996, ApJ, 457, 933

Hurlburt, N. E., & Rucklidge, A. M. 2000, MNRAS, 314, 793

Jain, R., Hindman, B. W., Braun, D. C., & Birch, A. C. 2009, ApJ, 695, 325

Keppens, R. 2001, in Encyclopedia of Astronomy and Astrophysics, ed. P. Murdin, (Bristol, IOP), 2043, DOI:10.1888/0333750888/2043

Keppens, R., & Martínez Pillet, V. 1996, A&A, 316, 229

Kubo, M., Lites, B. W., Ichimoto, K., Shimizu, T., Suematsu, Y., Katsukawa, Y., Tarbell, T. D., Shine, R. A., Title, A. M., Nagata, S., & Tsuneta, S. 2008, ApJ, 681, 1677

Leka, K. D., & Steiner, O. 2001, ApJ, 552, 354

Moradi, H., Baldner, C., Birch, A. C., Braun, D., Cameron, R., Duvall Jr., T. L., Gizon, L., Haber, D., Hanasoge, S., Jackiewicz, J., Khomenko, E., Komm, R., Rajaguru, P., Rempel, M., Roth, M., Schlichenmaier, R., Schunker, H., Spruit, H., Strassmeier, K., Thompson, M. J., & Zharkov S. 2010, arXiv:0912.4982v1 [astro-ph.SR]

Parchevsky, K. V., & Kosovichev, A. G. 2009, ApJ, 694, 573

Parker, E. N. 1979, ApJ, 230, 905

Petrovay, K, & Moreno-insertis, F. 1997, ApJ, 485, 398

Petrovay, K, & Van Driel-Gesztelyi, L. 1997, Sol. Phys., 176, 249

Rempel, M., Schüssler, M., Cameron, R. H., & Knölker, M. 2009a, Science, 325, 171

Rempel, M., Schüssler, M., & Knölker, M. 2009a, ApJ, 691, 640

Rimmele, T. R. 2004, ApJ, 604, 906

Rucklidge, A. M., Schmidt, H. U., & Weiss, N. O. 1995, MNRAS, 273, 491

Sankarasubramanian, K., & Rimmele, T. 2003, ApJ, 598, 689

Scharmer, G. B., Gudiksen, B. V., Kiselman, D., Löfdahl, M. G., & Rouppe van der Voort, L. H. M. 2002, Nature, 420, 151

Schlichenmaier, R., Jahn, K., & Schmidt, H. U. 1998, A&A, 337, 897

Shelyag, S., Zharkov, S., Fedun, V., Erdélyi, R., & Thompson, M. J. 2009, A&A, 501, 735

Shine, R. A., & Title, A. M. 2001, in Encyclopedia of Astronomy and Astrophysics, ed. Murdin, P., (Bristol: IOP Publishing), vol. 4, p. 3209, doi: 10.1888/0333750888/2038

Simon, G. W., & Leighton, R. B. 1964, ApJ, 140, 1120

Sobotka, M., Vázquez, M., Bonet, J. A., Hanslmeier, A., & Hirzberger, J. 1999, ApJ, 511, 436

Solanki, S. K. 2003, Astron Astrophys Rev, 11, 153

Stangl, S., & Hirzberger, J. 2005, A&A, 432, 319

Stein, R. F., & Nordlund, Å. 2006, ApJ, 642, 1246

Thomas, J. H., & Weiss, N. O. 2004, Annu. Rev. Astron. Astrophys., 42, 517

Tong C. H., 2005, Phil. Trans. R. Soc. A, 363, 2761

Tsuneta, S., Ichimoto, K., Katsukawa, Y., Lites, B. W., Matsuzaki, K., Nagata, S., Orozco Suárez, D., Shimizu, T., Shimojo, M., Shine, R. A., Suematsu, Y, Suzuki, T. K., Tarbell, T. D., & Title, A. M. 2008 ApJ, 688, 1374

Weiss, N. O. 1966, Proc. R. Soc. London A, 293, 310

Yang, G., Xu, Y., Wang, H., & Denker, C. 2003, ApJ, 597, 1190

Zhang, J., Lin, G., Wang, J., Wang, H., & Zirin, H. 1998, Sol. Phys., 178, 245

Zhao, J., Kosovichev, A. G., & Sekii, T. 2010, ApJ, 708, 304

Zwaan, C. 1992 in Thomas, J. H., & Weiss, N. O., eds, Sunspots: Theory and Observations, Cambridge University Press, Cambridge UK, p. 75

This 2-column preprint was prepared with the AAS LaTeX macros v5.2.

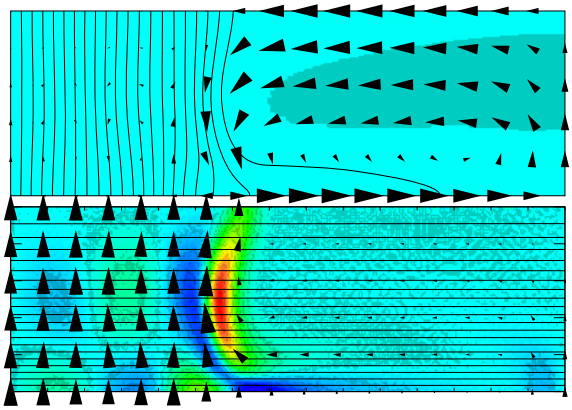

Fig. 1.— Initial axisymmetric state obtained with $Q = 100$ and $\Gamma = 3$. In the top panel the colour (grey in the printed version) represents the temperature fluctuation relative to the unperturbed state, the lines magnetic field and the arrows the velocity field. In the bottom panel the colour (grey in the printed version) represents azimuthal current density j_ϕ in the (r, z) plane, the arrows magnetic field and contours the mass density ρ. The axis is on the left hand edge of each panel.

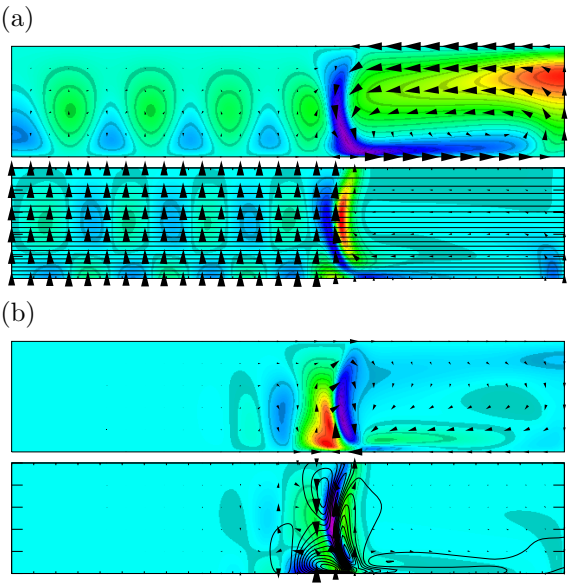

Fig. 2.— 3D state obtained with $Q = 500$ and $\Gamma = 5$. The solution is sampled at the vertical (r, z) plane taken at mid-sector with $M_\phi = 10$. (a) is the full solution and (b) the azimuthal perturbations of the physical quantities. In both (a) and (b) the top panel represents the temperature fluctuation relative to the unperturbed state in colour and the velocity field as arrows. In the bottom panel colour represents azimuthal current density j_ϕ, arrows the magnetic field and contours the mass density ρ. All colour scales are replaced by grey scales in the printed version. The solution forms an axisymmetric standing wave inside the magnetic flux bundle, and one annular convection cell round the flux bundle, as seen in (a). The linear modes are located at the boundary between the magnetic flux bundle and the convection cell, shown in (b). The amplitudes of the linear modes oscillate and this data set was sampled at maximum amplitude. The axis is on the left hand edge of each panel.

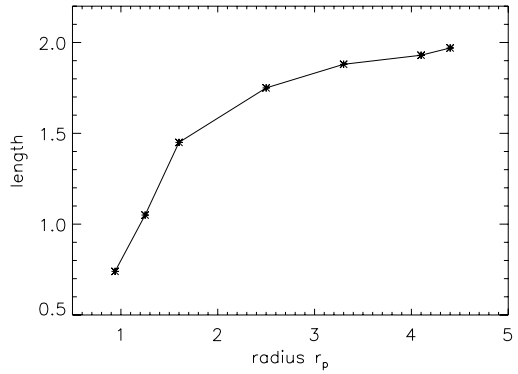

Fig. 3.— Length of linear modes in the azimuthal direction, for different magnetic flux tube radii (r_p). The length is calculated as $2\pi r_p/M_\phi$. The stars are the values measured from our simulations.

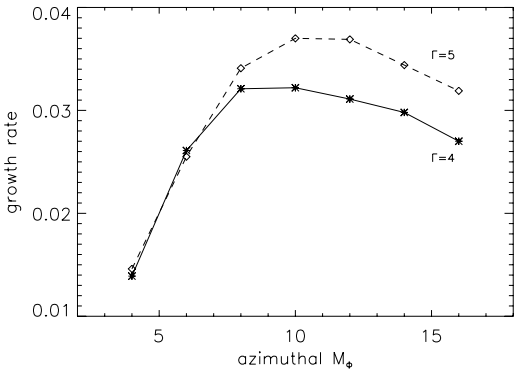

Fig. 4.— Linear growth rates measured for different M_ϕ with numerical domain radii of $\Gamma = 4$ (solid line) and $\Gamma = 5$ (broken line). The stars and diamonds are the values obtained from our simulations. These growth rates were obtained with a Chandrasekhar number $Q = 500$, chosen so that the thickness of the magnetic flux tube allows only one convection cell to form in the radial direction outside the flux tube.

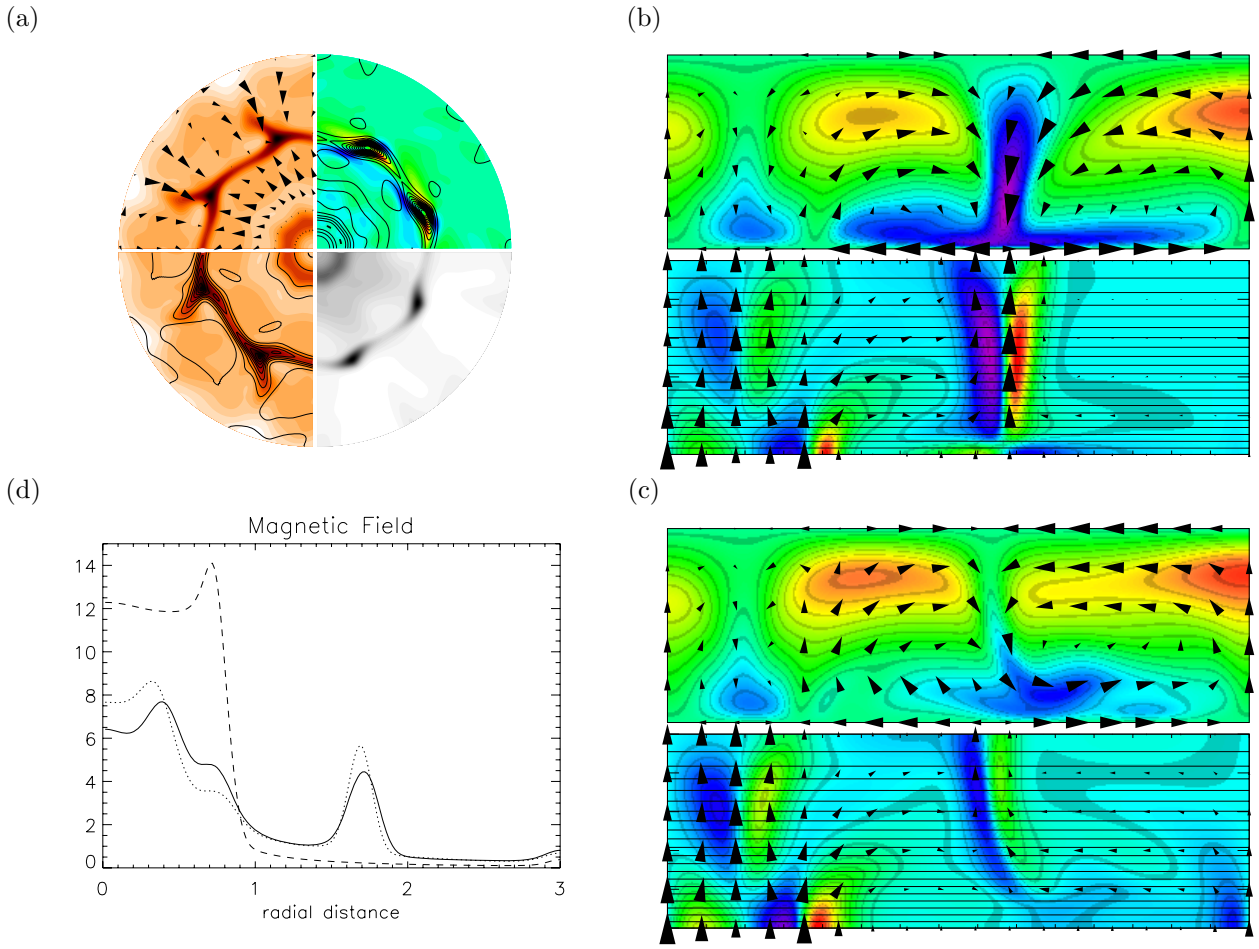

Fig. 5.— Nonlinear solution with $Q = 32$, $\Gamma = 3$ and $M_\phi = 8$ at time 1006.81. (a) shows the horizontal midplane, and the two vertical planes are sampled at (b) $\phi = 18°$ with $\max|\mathbf{B}| = 16.1$ and (c) $\phi = 45°$ with $\max|\mathbf{B}| = 12.5$. (d) represents the radial profile of the summed magnetic field, defined in (11), at three different times. The solid line is at time 1006.8, the dotted line at time 835.7 and the dashed line is the profile of the axisymmetric initial condition at time 328.0. The diagnostics for the horizontal plane (a) are as follows: in the first quadrant the colour represents j_z and the contours B_z; in the second quadrant the colour is the temperature fluctuation relative to the unperturbed state (dark is cold) and arrows are the velocity field; in the third quadrant the colour is the temperature fluctuation relative to the unperturbed state and contours are the mass density; in the fourth quadrant grey is magnetic field strength, with $\max|\mathbf{B}| = 15.4$ black and zero white. In the printed version the colour scales in quadrants one, two and three are printed as grey scales. The diagnostics for the two vertical planes are the same as in Figure 2(a). The physics in the two vertical planes are as follows: (b) has $\min(\beta) = 17.2$, $\max(\beta) = 1.6 \times 10^{11}$, $\min(j_\phi) = -118.8$, $\max(j_\phi) = 125.5$, $\min(\tilde{T}) = 0.98$, $\max(\tilde{T}) = 1.01$; (c) has $\min(\beta) = 29.6$, $\max(\beta) = 5.9 \times 10^{7}$, $\min(j_\phi) = -62.0$, $\max(j_\phi) = 80.3$, $\min(\tilde{T}) = 0.98$, $\max(\tilde{T}) = 1.01$. Here β is the ratio of gas pressure over magnetic pressure. In this solution max(Mach number) = 0.1.

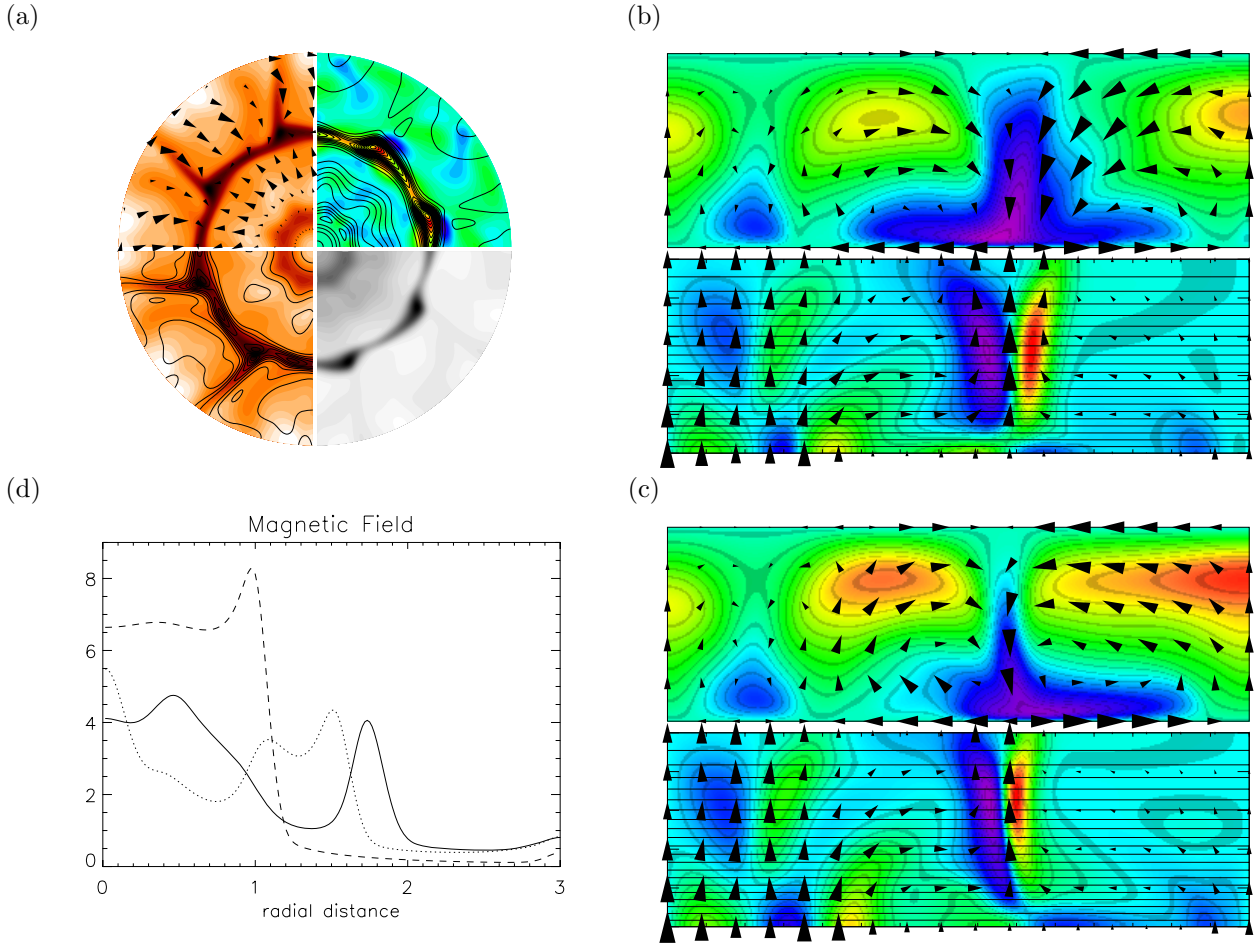

Fig. 6.— Nonlinear solution with $Q = 100$, $\Gamma = 3$ and $M_\phi = 8$ at time 1043.13. (a) shows the horizontal midplane with $\max|\mathbf{B}| = 9.4$, and the two vertical planes are sampled at (b) $\phi = 15°$ with $\max|\mathbf{B}| = 9.4$ and (c) $\phi = 45°$ with $\max|\mathbf{B}| = 7.9$. (d) represents the radial profile of the summed magnetic field, defined in (11), at three different times. The solid line is at time 1043.13, the dotted line at time 803.5 and the dashed line is the profile of the axisymmetric initial condition at time 357.1. The diagnostics for the horizontal plane (a) are the same as in Figure 5 and for the two vertical planes as in Figure 2(a). The physics in the two vertical planes are as follows: (b) has $\min(\beta) = 15.8$, $\max(\beta) = 7.4\times10^{10}$, $\min(j_\phi) = -54.8$, $\max(j_\phi) = 62.7$, $\min(\tilde{T}) = 0.99$, $\max(\tilde{T}) = 1.01$; (c) has $\min(\beta) = 28.0$, $\max(\beta) = 1.2 \times 10^7$, $\min(j_\phi) = -46.2$, $\max(j_\phi) = 51.7$, $\min(\tilde{T}) = 0.99$, $\max(\tilde{T}) = 1.01$. In this solution max(Mach number) = 0.1.

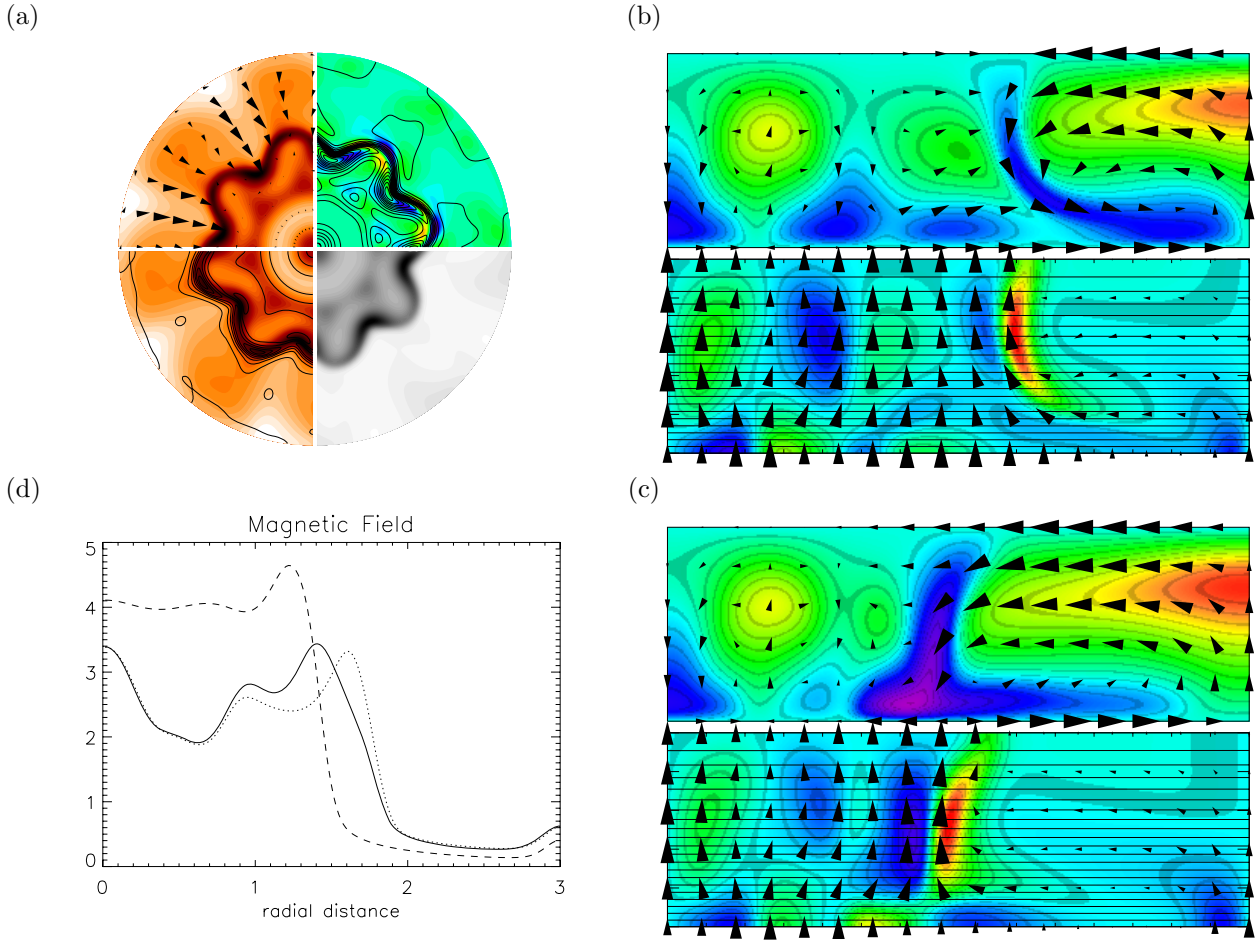

Fig. 7.— Nonlinear solution with $Q = 250$, $\Gamma = 3$ and $M_\phi = 8$ at time 1034.95. (a) shows the horizontal midplane with $\max|\mathbf{B}| = 6.4$, and the two vertical planes are sampled at (b) $\phi = 10°$ with $\max|\mathbf{B}| = 4.4$ and (c) $\phi = 35°$ with $\max|\mathbf{B}| = 6.4$. (d) represents the radial profile of the summed magnetic field, defined in (11), at three different times. The solid line is at time 1034.95, the dotted line at time 794.98 and the dashed line is the profile of the axisymmetric initial condition at time 471.34. The diagnostics for the horizontal plane (a) are the same as in Figure 5 and for the two vertical planes as in Figure 2(a). The physics in the two vertical planes are as follows: (b) has $\min(\beta) = 24.2$, $\max(\beta) = 1.2 \times 10^7$, $\min(j_\phi) = -16.3$, $\max(j_\phi) = 32.6$, $\min(\tilde{T}) = 0.99$, $\max(\tilde{T}) = 1.01$; (c) has $\min(\beta) = 13.8$, $\max(\beta) = 7.7 \times 10^{12}$, $\min(j_\phi) = -25.7$, $\max(j_\phi) = 45.5$, $\min(\tilde{T}) = 0.99$, $\max(\tilde{T}) = 1.01$. In this solution max(Mach number) = 0.1.

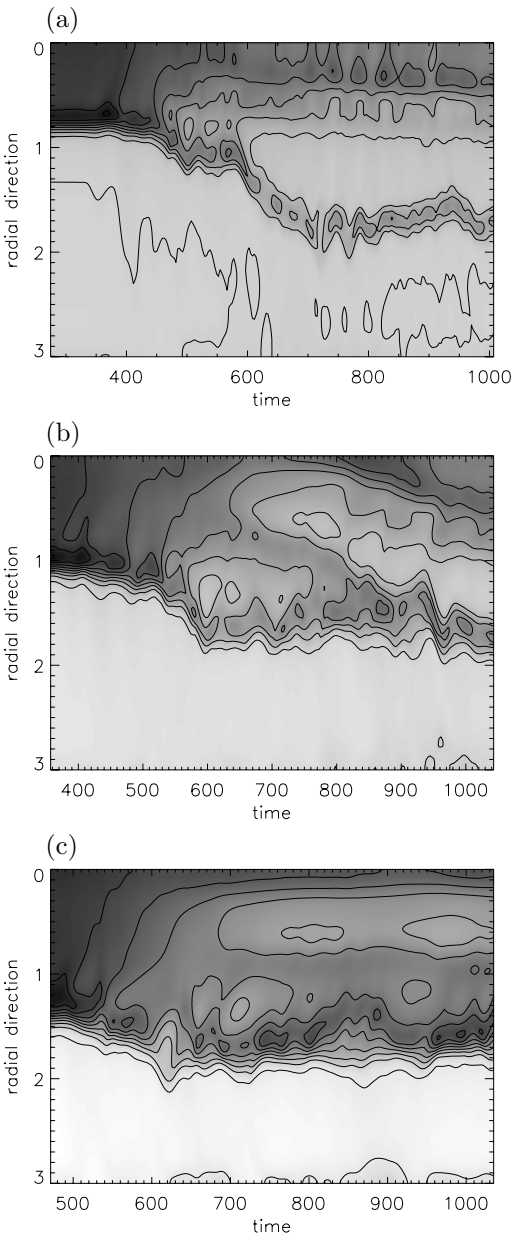

Fig. 8.— The time evolution of the summed magnetic field as defined in (11). Black represents $\max|\bar{B}|$ and white zero. The spatial dimensions are $\Gamma = 3$ and $M_\phi = 8$. The axis is along the top edge of each panel, and the time begins when the nonaxisymmetric perturbations are introduced. (a) presents $Q = 32$ with $\max|\bar{B}| = 15.22$, of which three instances are plotted in Figure 5(d). (b) presents $Q = 100$ with $\max|\bar{B}| = 8.27$, of which three instances are plotted in Figure 6(d). (c) presents $Q = 250$ with $\max|\bar{B}| = 4.64$, of which three instances are plotted in Figure 7(d). The convection tears magnetic flux away from the the central flux bundle in the cases of $Q = 32$ and $Q = 100$, while the flux bundle stays intact for $Q = 250$.

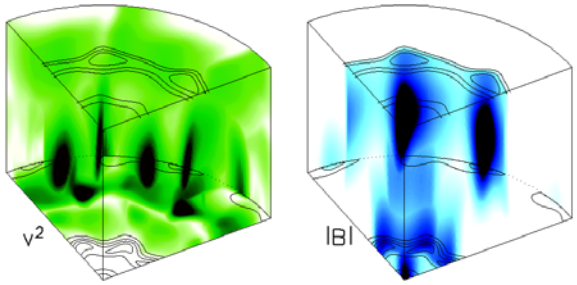

Fig. 9.— A 3D rendering of the kinetic and magnetic energies in the system, with $Q = 100$, $\Gamma = 3$ and $M_\phi = 8$. The physical parameters are given in Figure 6. On the left hand side is the velocity field (v^2) in green and on the right hand side the magnetic field $|\mathbf{B}|$ in blue. A grey scale is used in the printed version. The contours at the top and bottom panels of the wedge are the vertical magnetic field passing through these planes.

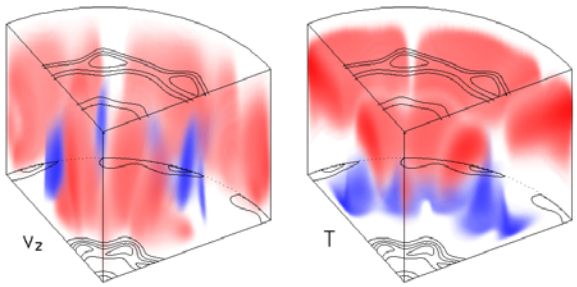

Fig. 10.— The vertical velocity perturbation on each plane ($\tilde{v}_z$) on the left hand side and the temperature perturbation on each plane ($\tilde{T}$) on the right hand side. The velocity is colour coded so that upward flow is red and downward flow blue. For the temperature red shows where the plasma is hot and blue where it is cool relative to the surrounding temperature. In the printed version only the upflow and hot plasma are shown in a grey scale. The physical parameters are as in Figure 6, with $Q = 100$, $\Gamma = 3$ and $M_\phi = 8$. The contours at the top and bottom panels of the wedge are the vertical magnetic field passing through these planes.

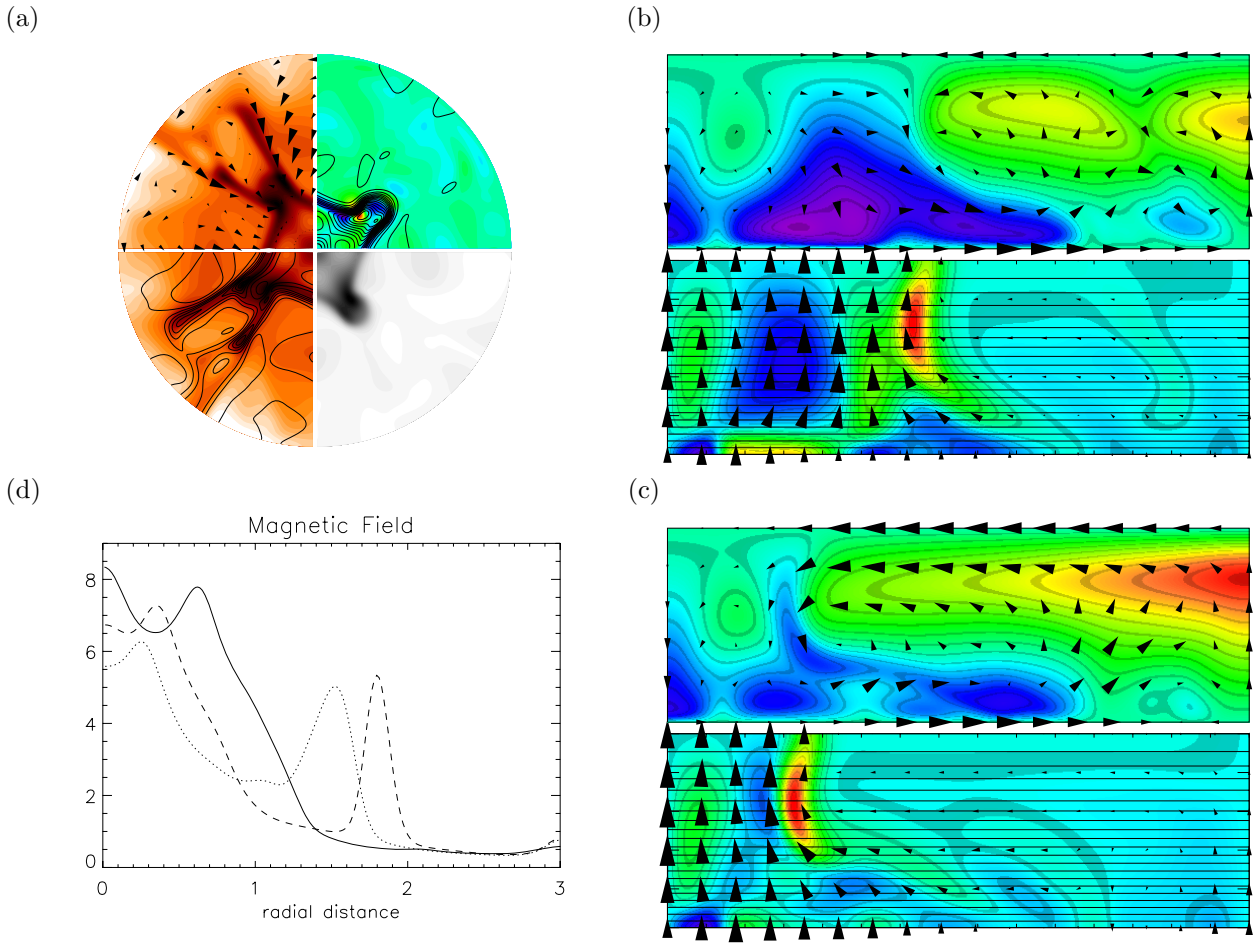

Fig. 11.— Nonlinear solution with $Q = 32$, $\Gamma = 3$ and $M_\phi = 4$ at time 1208.72. This simulation was initialised from the numerical run depicted in Figure 5, with a data set taken at time 799.42. (a) shows the horizontal midplane with $\max|\mathbf{B}| = 12.2$, and the two vertical planes are sampled at (b) $\phi = 35°$ with $\max|\mathbf{B}| = 15.0$ and (c) $\phi = 70°$ with $\max|\mathbf{B}| = 9.9$. (d) represents the radial profile of the summed magnetic field, defined in (11), at three different times. The solid line is at time 1208.72, the dotted line at time 1011.39 and the dashed line at time 800.23. The diagnostics for the horizontal plane (a) are the same as in Figure 5 and for the two vertical planes as in Figure 2(a). The physics in the two vertical planes are as follows: (b) has $\min(\beta) = 17.2$, $\max(\beta) = 7.6 \times 10^{11}$, $\min(j_\phi) = -44.4$, $\max(j_\phi) = 68.6$, $\min(\tilde{T}) = 0.98$, $\max(\tilde{T}) = 1.01$; (c) has $\min(\beta) = 27.1$, $\max(\beta) = 2.5 \times 10^{11}$, $\min(j_\phi) = -45.7$, $\max(j_\phi) = 77.7$, $\min(\tilde{T}) = 0.98$, $\max(\tilde{T}) = 1.01$. In this solution max(Mach number) = 0.03 in (b) and 0.09 in (c).

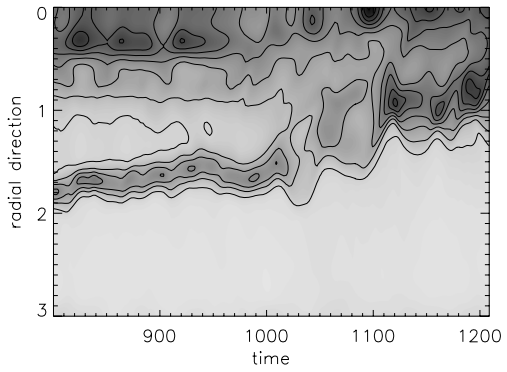

Fig. 12.— The time evolution of the summed magnetic field as defined in (11) for $Q = 32$, $\Gamma = 3$ and $M_\phi = 4$, with black representing $\max|\bar{B}| = 11.58$ and white zero. The axis is along the top edge of the panel. Three instances from this data set are plotted in Figure 11(d). The coalescing of the magnetic flux at the central axis is clearly visible.

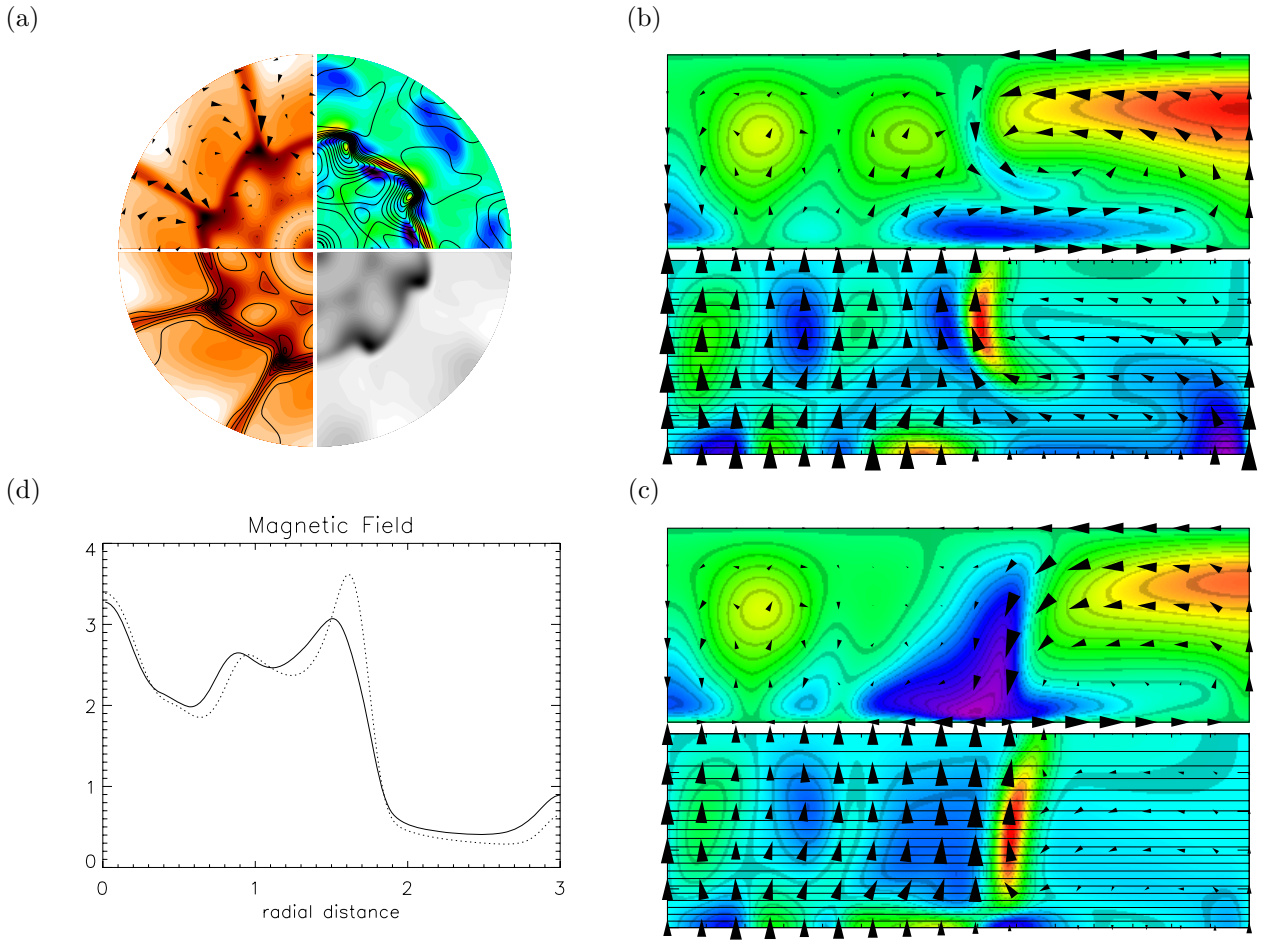

Fig. 13.— Nonlinear solution with $Q = 250$, $\Gamma = 3$ and $M_\phi = 4$ at time 901.03. This simulation was initialised from the numerical run depicted in Figure 7, with a data set taken at time 800.83. The solution retains its $M_\phi = 8$ structure. (a) shows the horizontal midplane with $\max|\mathbf{B}| = 4.6$, and the two vertical planes are sampled at (b) $\phi = 5°$ with $\max|\mathbf{B}| = 4.2$ and (c) $\phi = 30°$ with $\max|\mathbf{B}| = 6.4$. (d) represents the radial profile of the summed magnetic field, defined in (11), at two different times. The solid line is at time 901.03, the dotted line at time 801.64. The diagnostics for the horizontal plane (a) are the same as in Figure 5 and for the two vertical planes as in Figure 2(a). The physics in the two vertical planes are as follows: (b) has $\min(\beta) = 27.2$, $\max(\beta) = 1.2 \times 10^6$, $\min(j_\phi) = -25.5$, $\max(j_\phi) = 28.6$, $\min(\tilde{T}) = 0.98$, $\max(\tilde{T}) = 1.01$; (c) has $\min(\beta) = 13.5$, $\max(\beta) = 2.8 \times 10^9$, $\min(j_\phi) = -22.4$, $\max(j_\phi) = 48.5$, $\min(\tilde{T}) = 0.98$, $\max(\tilde{T}) = 1.01$. In this solution max(Mach number) = 0.07 in (b) and 0.06 in (c).

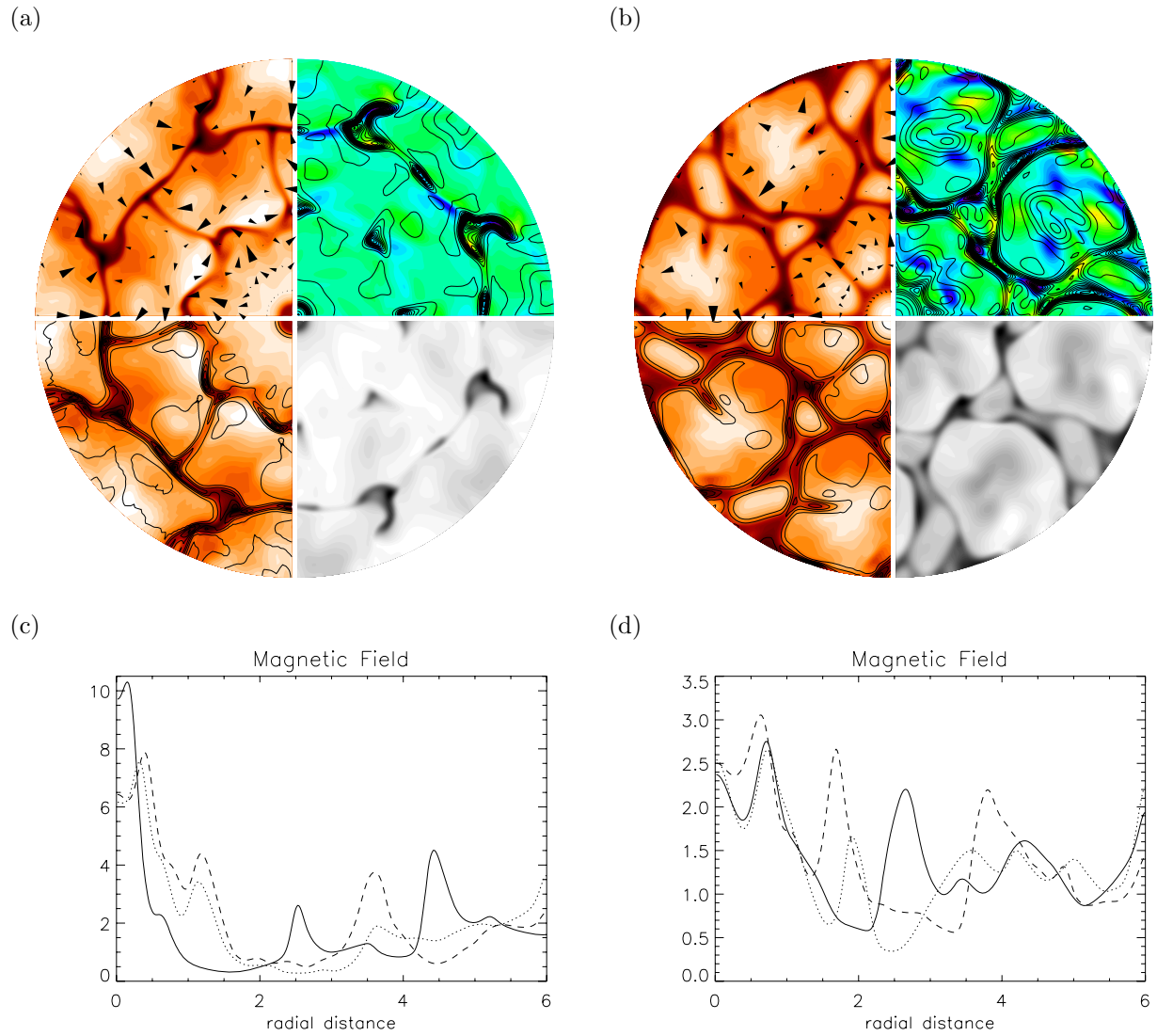

Fig. 14.— Nonlinear solutions with $\Gamma = 6$ and $M_\phi = 8$. The horizontal midplanes are shown for (a) $Q = 32$ at time 1509.8 with $\max|\mathbf{B}| = 13.1$ and (b) $Q = 250$ at time 2679.2 with $\max|\mathbf{B}| = 5.6$. The diagnostics for the horizontal planes are the same as in Figure 5. The radial profiles of the summed magnetic field, defined in (11), for these nonlinear solutions are given below each solution. (c) is for $Q = 32$ with the solid line at time 1509.8, the dotted line at time 1228.5 and the broken line at time 946.49. (d) is for $Q = 250$ with the solid line at time 2679.2, the dotted line at time 2368.79 and the broken line at time 2086.24.

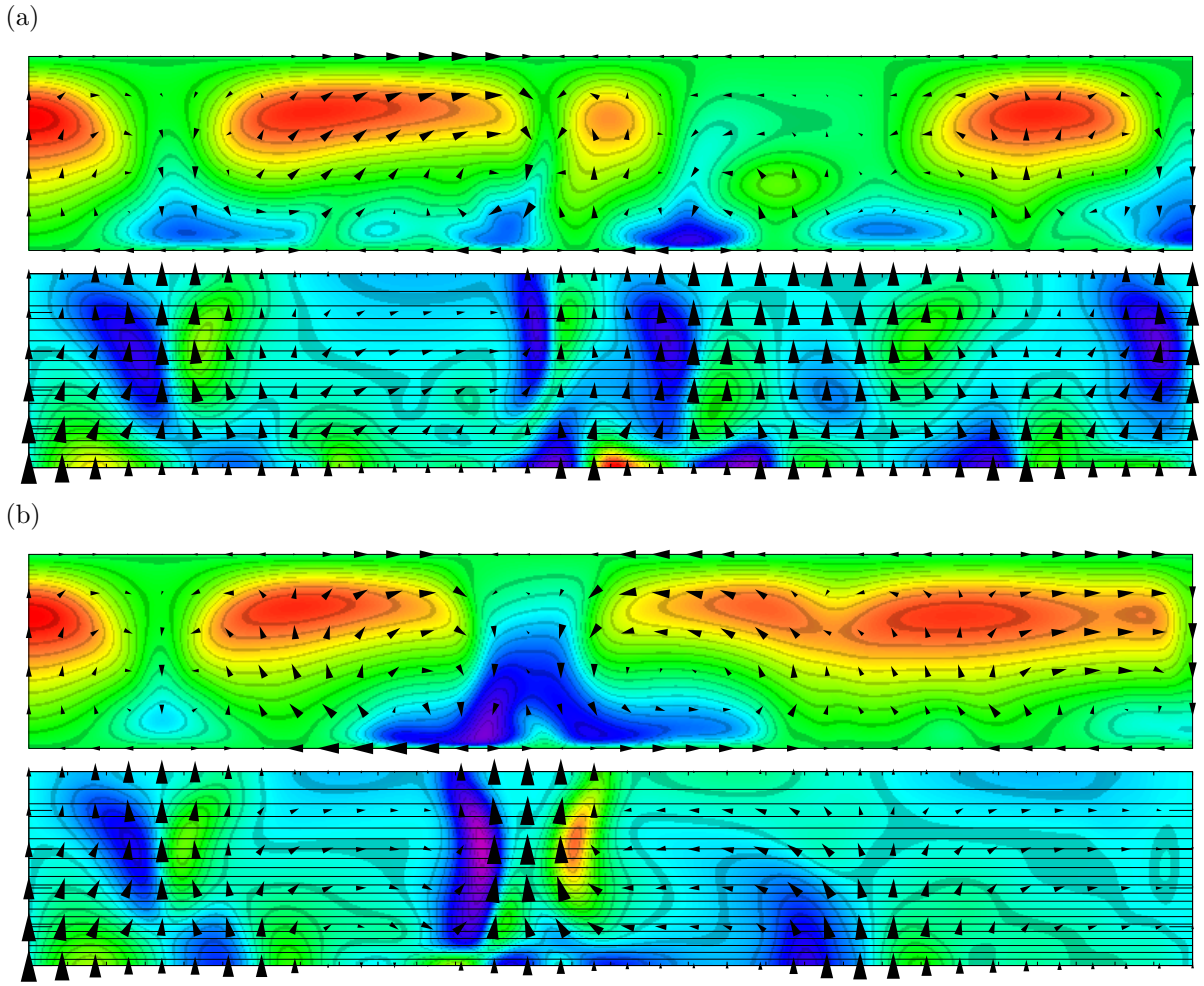

Fig. 15.— Vertical planes of nonlinear solution in Figure 14(b) for $Q = 250$, $\Gamma = 6$ and $M_\phi = 8$, sampled at (a) $\phi = 10°$ with $\max|\mathbf{B}| = 5.3$ and (b) $\phi = 35°$ with $\max|\mathbf{B}| = 5.6$. The diagnostics for the vertical planes are the same as in Figure 2(a). The physics are as follows: (a) has $\min(\beta) = 21.1$, $\max(\beta) = 4.6 \times 10^5$, $\min(j_\phi) = -6.9$, $\max(j_\phi) = 8.4$, $\min(\tilde{T}) = 0.98$, $\max(\tilde{T}) = 1.01$; (b) has $\min(\beta) = 15.0$, $\max(\beta) = 1.5 \times 10^{12}$, $\min(j_\phi) = -26.6$, $\max(j_\phi) = 23.6$, $\min(\tilde{T}) = 0.98$, $\max(\tilde{T}) = 1.01$. In this solution max(Mach number) = 0.05.

(a)

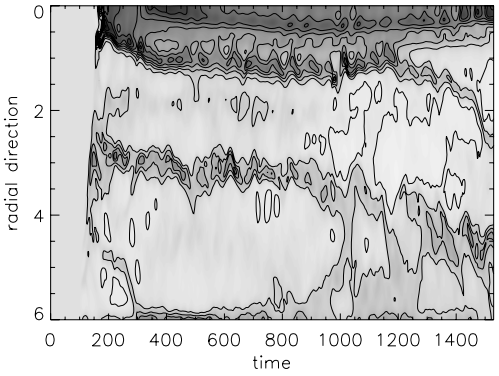

(b)

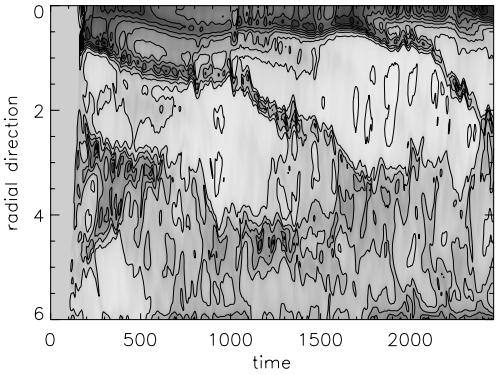

(c)

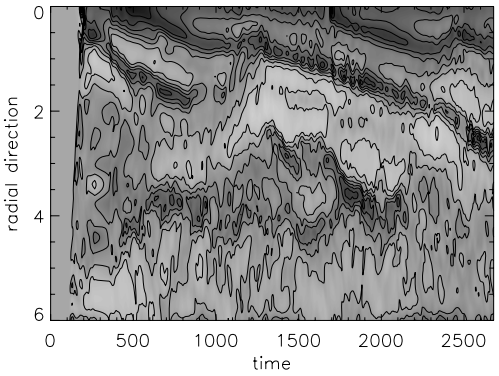

Fig. 16.— The time evolution of the summed magnetic field as defined in (11). Black represents $\max|\bar{B}|$ and white zero. The spatial dimensions are $\Gamma = 6$ and $M_\phi = 8$. The axis is along the top edge of each panel. (a) presents $Q = 32$ with $\max|\bar{B}| = 12.09$, of which three instances are plotted in Figure 14(c) (b) presents $Q = 100$ with $\max|\bar{B}| = 6.78$. (c) presents $Q = 250$ with $\max|\bar{B}| = 3.91$, of which three instances are plotted in Figure 14(d) Throughout the simulations magnetic flux is eroded from the central axis by the convection.